



Numerical analysis of beam self-cleaning in multimode fiber amplifiers

MESAY ADDISU JIMA,^{1,2} ALESSANDRO TONELLO,² ALIOUNE NIANG,^{3,4}
TIGRAN MANSURYAN,² KATARZYNA KRUPA,⁵ DANIELE MODOTTO,^{1,*}
ANNAMARIA CUCINOTTA,⁶ VINCENT COUDERC,² AND STEFAN WABNITZ^{3,7}

¹Dipartimento di Ingegneria dell'Informazione, Università di Brescia, via Branze 38, 25123 Brescia, Italy

²Université de Limoges, XLIM, UMR CNRS 7252, 123 Av. A. Thomas, 87060 Limoges, France

³Dipartimento di Ingegneria dell'Informazione, Elettronica e Telecomunicazioni, Sapienza Università di Roma, via Eudossiana 18, 00184 Rome, Italy

⁴Current address: Computer Science and Electrical Engineering Department, University of Maryland, Baltimore, Maryland 21250, USA

⁵Institute of Physical Chemistry Polish Academy of Sciences, ul. Kasprzaka 44/52, 01-224 Warsaw, Poland

⁶Dipartimento di Ingegneria e Architettura, Università di Parma, Parco Area delle Scienze 181/A, I-43124 Parma, Italy

⁷CNR-INO, Istituto Nazionale di Ottica, Via Campi Flegrei 34, 80078 Pozzuoli (NA), Italy

*Corresponding author: daniele.modotto@unibs.it

Received 9 May 2022; revised 19 June 2022; accepted 20 June 2022; posted 21 June 2022; published 21 July 2022

Recent experimental results have reported the observation of beam self-cleaning or, more generally, nonlinear beam reshaping in active multimode fibers. In this work, we present a numerical analysis of these processes by considering the ideal case of a diode-pumped signal amplifier made of a graded-index multimode fiber with uniform Yb doping. Simulations confirm that beam cleaning of the signal may take place even in amplifying fibers, in the absence of beam power conservation. Moreover, we show how the local signal intensity maxima, which are periodically generated by the self-imaging process, may influence the population inversion of the doping atoms, and locally saturate the amplifier gain. © 2022 Optica Publishing Group

<https://doi.org/10.1364/JOSAB.463473>

1. INTRODUCTION

Light propagation in active waveguides may hold surprises or counterintuitive situations. An example is provided by the robust single-mode behavior that can be obtained in the presence of sufficiently large gain, even in step-index fibers with a refractive index dip in the core, or in antiguides [1]. Doped fibers provide the most technologically successful and suitable platform for optical amplifiers. Accurate models to describe short pulse propagation in active fibers, including the contribution to dispersion introduced by the active ions, have been developed; see, for instance, Ref. [2].

In this context, Yb-doped fibers are of particular interest for many applications, since their quantum defect is small, which contributes to reducing thermal effects, and allows for developing high-power amplifiers and lasers, especially if large-mode-area or multimode (MM) fibers are used. A thorough discussion of Yb-doped fiber amplifiers can be found in Ref. [3], whereas static and dynamic instabilities due to thermo-optic effects are analyzed in Refs. [4,5].

An interesting aspect is that, in a MM fiber amplifier, the beating among modes can create a thermally induced refractive index grating, which in turn leads to modal energy transfer and causes the well-known transverse mode instabilities [6]. The

amplification of coherent signals in MM fiber amplifiers cannot be merely limited to the study of their overall power throughput; it is essential to consider transversally resolved rate equations, since the light intensity pattern can lead to different amplification regimes, and it has a substantial impact on the quality of the output beam [7].

Remarkably, steering of the output beam from an MM active fiber could be obtained by properly shaping the input beam phase front via a spatial light modulator (such as a segmented deformable mirror). This was achieved by measuring the relevant transmission matrix and by implementing appropriate wavefront control algorithms [8,9].

On the other hand, in recent years, there has been a resurgence of research interest in nonlinear optical effects in MM fibers. Among these, spatial beam self-cleaning (BSC) due to intermodal four-wave mixing via the Kerr effect was first observed in passive graded-index (GRIN) fibers [10]. Soon thereafter, BSC was also reported in an Yb-doped fiber amplifier with a quasi-step-index profile [11]. Although the radial evolution of the refractive index profile was not following a parabolic profile, it was possible to observe BSC at 1064 nm, both in the presence or in the absence of an additional forward diode pump at 940 nm, leading to signal gain of about 13 dB [11], or to a signal loss of 7.3 dB owing to Yb ground state absorption,

respectively. This experimental work was also extended, for a quasi-step index MM fiber, to the case of a coupled-cavity-composite MM laser [12] and, more recently, to Yb-doped fiber tapers with GRIN profiles [13,14]. Note that nonlinear MM propagation in passive GRIN fibers has been theoretically and experimentally studied in recent years in the frame of wave turbulence and thermodynamic descriptions of conservative wave systems [15–21]. The numerical simulation of complex beam shaping combining MM propagation, gain/loss mechanisms, and the Kerr effect has recently been discussed in the context of spatiotemporal mode-locked fiber lasers [22,23]. This has permitted researchers to point out the role played by gain saturation as a modal coupling mechanism for locking both longitudinal and transverse laser modes (see supplementary material of Ref. [22]). In addition, the generation of self-similar pulses in all-normal dispersion mode-locked fiber lasers has been experimentally and numerically studied in Ref. [24].

In this work, we introduce a numerical model, suitable for describing spatial beam-cleaning effects in active GRIN MM fibers. Our simulation results fully support earlier experimental findings using Yb-doped MM fibers, showing that dissipative MM fibers are a convenient and important platform for obtaining BSC. Moreover, our model permits us to design and optimize novel active fiber structures and amplification schemes based on BSC, for example, by introducing a suitable transverse gain/loss distribution in the fiber core. Our study is organized as follows: Section 2 explains the mathematical model for gain in Yb-doped MM fibers; Sections 3 and 4 describe the dynamics in Yb-doped MM fibers, both in the absence of any pumping, and with a forward pump, respectively; Section 5 extends the analysis of BSC and self-imaging to Yb-doped MM tapers; finally, Section 6 draws our conclusions.

2. DISTRIBUTED GAIN MODEL

Our goal is to numerically study signal beam evolution in Yb-doped MM fibers under the combined action of the Kerr effect and gain due to Yb ions, with continuous wave (CW) diode pumping. For efficient pumping, we consider a double cladding active fiber structure: owing to the presence of thousands of modes in the inner cladding, the pump distribution is uniform in the transverse dimension.

Previous experiments with either passive [10] or active MM fibers [11] have taught us that, when using signal powers higher than a few tens of kilowatts, a reshaping of the transverse beam profile is obtained after 2–3 m of propagation. As a matter of fact, as the signal power grows larger, one observes a progressive evolution of the output speckled pattern, which is typical of the MM regime, towards a single bell-shaped profile. For such a reason, our numerical model must necessarily include, besides the dependence of the field on the transverse coordinates, a longitudinal fiber perturbation that breaks the radial symmetry of the beam and leads, in the linear regime, to a speckled output pattern as a result of MM interference [15,16,19]. We underline that the signal evolution cannot be only modeled in terms of mode powers, since keeping track of the phase evolution is necessary for properly modeling linear and nonlinear mode coupling.

The model presented herein combines transversally resolved rate equations, including the pump power $P_p(z)$, with a nonlinear beam propagation equation for the signal electric field $E(x, y, z)$. In the present work, for the ease of discussion, we limit our analysis to the scalar approximation, and neglect the polarization effects (Refs. [15,16,25]). When considering forward pumping, the pump evolution is described by the equation

$$\frac{dP_p}{dz} = \left[(\sigma_{AP} + \sigma_{EP}) \frac{\int_S N_2(x, y, z) dS}{A_{Cl}} - \sigma_{AP} \frac{\int_S N_T(x, y) dS}{A_{Cl}} \right] P_p - \alpha_P P_p, \quad (1)$$

where σ_{AP} and σ_{EP} are absorption and emission cross sections at the pump wavelength, N_1 (N_2) is the ground (excited) Yb ion density, $N_T = N_1 + N_2$ is the total Yb density, A_{Cl} is the inner cladding area, and α_P is the linear pump absorption coefficient. Since we consider a uniformly distributed pump (i.e., it does not depend on x, y) in the inner guiding cladding, the pump intensity reads as $I_p(z) = P_p(z)/A_{Cl}$. In the previous equation, the local densities of ions in the ground and excited states depend on the three spatial coordinates, since, as we will see, it is important to take into account the fact that N_1 and N_2 vary not only along the longitudinal coordinate z , but also in the transverse x, y plane. As a result, the two integrals for the ion densities are calculated on the cross section S , where doping is present. In this work, we assume that doping is only present in the core, where it is uniformly distributed. Therefore, N_T is constant, and it vanishes outside the core.

The pump is CW, and we consider the steady-state amplification regime. Nevertheless, when writing the rate equations, we must take into account that the signal pulses have a duration T_S , a repetition rate $1/T_R$ (where T_R is the separation between two consecutive pulses), and a time-dependent intensity $I_S(x, y, z, t)$. We can define the time-averaged signal intensity as $\bar{I}_S(x, y, z) = 1/T_R \int_{T_R} I(x, y, z, t) dt \simeq \max_t [I(x, y, z, t)] T_S/T_R$: this is an approximation in this context, although it is often adopted in fiber lasers [26]. It follows that the density of excited ions $N_2(x, y, z)$ can be explicitly written as a function of the pump and the (time-averaged) signal intensities [5],

$$N_2(x, y, z) = \frac{N_T (\sigma_{AP} I_p(z) + \sigma_{AS} \bar{I}_S(x, y, z) \lambda_S / \lambda_P)}{\sigma_{AEP} I_p(z) + \sigma_{AES} \bar{I}_S(x, y, z) \lambda_S / \lambda_P + P_\tau}, \quad (2)$$

where $\sigma_{AEP} = \sigma_{AP} + \sigma_{EP}$, $\sigma_{AES} = \sigma_{AS} + \sigma_{ES}$, τ is the excited level lifetime, $P_\tau = hc / (\lambda_P \tau)$, h is the Planck's constant, and c is the speed of light.

The complex envelope of the signal electric field $E(x, y, z)$ is normalized in such a way that its intensity is $I(x, y, z) = |E(x, y, z)|^2$; the field evolution is governed by the following equation [5]:

$$\frac{\partial E}{\partial z} = \frac{i}{2k_0} \{ \nabla_\perp^2 E + [k^2 - k_0^2] E \} + i\gamma |E|^2 E - \frac{\alpha_S}{2} E + \frac{1}{2} [(\sigma_{AS} + \sigma_{ES}) N_2 - \sigma_{AS} N_T] E, \quad (3)$$

where $k_0 = 2\pi n_0/\lambda_S$ is the reference propagation constant, $k = 2\pi n(x, y)/\lambda_S$, and $n(x, y)$ is the refractive index distribution. For an ideal GRIN fiber, $n(x, y)$ is well approximated by a circular paraboloid $n^2 = n_0^2(1 - 2\Delta \frac{x^2+y^2}{R^2})$, where the reference index is the maximum core refractive index $n_0 = n_{Co}$, n_{Cl} is the cladding index, and $\Delta = (n_{Co}^2 - n_{Cl}^2)/2n_{Co}^2$. In Eq. (3), the term in braces describes diffraction and the guiding structure, the term $i\gamma|E|^2E$ represents the instantaneous Kerr nonlinearity, α_S is the linear loss coefficient of the silica glass host, and the last term accounts for the gain $g(x, y, z)$ introduced by the population inversion, which reads as

$$g(x, y, z) = (\sigma_{AS} + \sigma_{ES})N_2(x, y, z) - \sigma_{AS}N_T(x, y, z). \quad (4)$$

It is worth observing that even if the Kerr coefficient and the doping are homogeneous over the fiber cross section, the intensity-dependent refractive index and the gain function depend on the transverse coordinates and can lead to an exchange of power among modes carried by the MM fiber. Equations (1) and (3) can be numerically solved with a split-step Fourier method. Moreover, the refractive index distribution can be perturbed by the population inversion of the Yb ions. The variation of the refractive index δn depends linearly on the population of the excited state, as described by the equation

$$\delta n = \frac{2\pi}{n_0} \left(\frac{n_0^2 + 2}{3} \right)^2 \Delta p N_2, \quad (5)$$

where $\Delta p = 1.2 \times 10^{-26} \text{ cm}^3$ is the polarizability difference of the Yb^{3+} ions in the excited and ground states, respectively [27]. We also assume that the Yb-doped glass, for the selected pump and signal wavelengths, behaves as a quasi-three-level system [28,29], and that the maximum fraction of inverted population is $N_2/N_T = 0.5$ (since $\sigma_{AP} = \sigma_{EP}$): by considering $N_T = 9 \times 10^{19} \text{ cm}^{-3}$ and a maximally inverted population $N_2 = 4.5 \times 10^{19} \text{ cm}^{-3}$, the resulting variation is $\delta n = 4.44 \times 10^{-6}$. In other words, $\delta n = 8.88 \times 10^{-6} N_2/N_T$, where N_2/N_T is the fractional inverted population. In GRIN fibers, the self-imaging effect is responsible for the formation of a Kerr-induced index grating [30,31], which also leads to a periodic modulation of N_2 according to Eq. (2), hence of δn .

In order to investigate how this refractive index modulation eventually interferes with the Kerr-induced index grating, in Eq. (3) we may replace $n(x, y)$ by $n(x, y) + \delta n(x, y, z)$: this part of the study is addressed at the end of Section 5. It is also worth observing that a local change in the fiber temperature δT of just a few Kelvin can lead to an increase in the refractive index, which is larger than that expected from population inversion, since $\delta n \simeq 1.2 \times 10^{-5} \delta T$; however, this would lead to refractive index fluctuations on a longitudinal scale that is longer than the self-imaging period. We may thus neglect this contribution in the current numerical analysis, and we plan to address this issue in subsequent studies.

It is also customary to express the guided signal field by using the base provided by the set of Hermite–Gauss guided modes $\psi_{h,k}(x, y)$, which are the eigensolutions of the linear problem $\nabla_{\perp}^2 E + [k^2 - k_0^2]E = 0$ for the GRIN fiber [32].

In the next sections, we develop our simulations for an ideal sample case, whose set of parameter values are summarized for simplicity in Table 1. Whenever necessary, in some simulations

the parameters will be modified (for instance, we may neglect the Kerr effect), as explained in the corresponding sections.

The disorder along the propagation, which is responsible for the formation of a speckled output intensity pattern in the linear regime, and which may also lead to an acceleration of the beam-cleaning process in the nonlinear regime [15], is implemented in the GRIN fiber with a core radius $R = 26 \mu\text{m}$ and $\Delta = 8.8 \times 10^{-3}$ by considering randomly oriented elliptical deformations of the fiber core, with a maximum excursion of the axes of $0.15 \mu\text{m}$, and a coarse 5 mm pitch for the ellipse rotation.

3. LINEAR AND NONLINEAR DYNAMICS IN Yb^{3+} -DOPED FIBER IN THE ABSENCE OF PUMPING

First, by means of an example, we numerically confirm that, whenever the input beam peak intensity grows larger than a certain threshold value, spatial BSC can indeed be obtained in an undoped, passive GRIN fiber.

Let us consider the parameters of Table 1 and an input Gaussian signal beam with a peak intensity in the time domain of 5 GW/cm^2 . The corresponding numerically calculated evolution [see the iso-intensity surface at half-maximum intensity in Fig. 1(a)] shows that a transition, from a wide and speckled intensity pattern into a cleaned beam, occurs after about 0.5 m . With 10 times less input intensity [see Fig. 1(b)], this beam-cleaning effect substantially vanishes: the transverse pattern remains speckled over the full propagation distance of 4 m , as it occurs when the simulation is carried out in the absence of the Kerr effect (i.e., we set $n_2 = 0$).

When one includes a uniform Yb doping (while keeping the same GRIN profile), and in the absence of a pump, i.e., with $P_P(0) = 0$, the GRIN fiber exhibits high losses, owing to ground state absorption by Yb ions. Nevertheless, quite surprisingly, Fig. 2 shows that, in spite of the additional loss, it is still possible to observe BSC in a doped unpumped fiber, with the same input signal peak intensity of 5 GW/cm^2 [see panel (a)]

Table 1. Parameters Used in Modeling and Numerical Simulations

Symbol	Parameter	Value
λ_P	pump wavelength	979 nm
λ_S	signal wavelength	1064 nm
T_S	signal pulse duration	500 ps
D	signal beam diameter FWHMI	40 μm
σ_{AP}	pump absorption cross section	$2.358 \times 10^{-24} \text{ m}^2$
σ_{EP}	pump emission cross section	$2.358 \times 10^{-24} \text{ m}^2$
σ_{AS}	signal absorption cross section	$5 \times 10^{-27} \text{ m}^2$
σ_{ES}	signal emission cross section	$2.89 \times 10^{-25} \text{ m}^2$
α_P	linear absorption (pump)	1.1 dB/km
α_S	linear absorption (signal)	1.1 dB/km
τ	radiative lifetime	1 ms
N_T	Yb^{3+} concentration	$9.0 \times 10^{25} \text{ m}^{-3}$
n_{Co}	maximum core refractive index	1.47
n_{Cl}	cladding refractive index	1.457
R	core radius	26 μm
A_{Cl}	inner cladding area	$7.06 \times 10^{-8} \text{ m}^2$
n_2	Kerr nonlinear coefficient	$2.6 \times 10^{-20} \text{ m}^2/\text{W}$

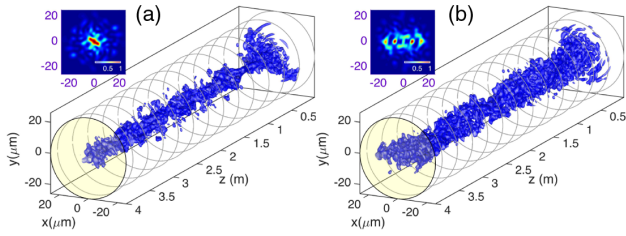


Fig. 1. (a) Beam cleaning in a passive GRIN fiber with input signal peak intensity 5 GW/cm^2 ; (b) propagation with input signal peak intensity 0.5 GW/cm^2 .

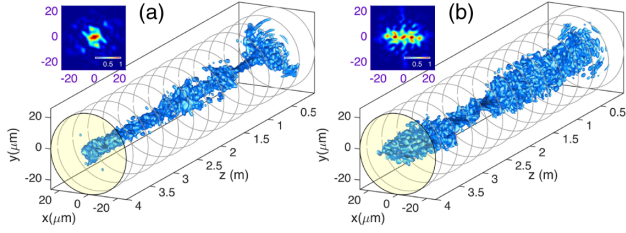


Fig. 2. (a) Beam cleaning in a nonlinear Yb-doped GRIN fiber, in the absence of pump for an input signal maximum intensity 5 GW/cm^2 ; (b) same propagation after turning off the Kerr effect ($n_2 = 0$).

as in Fig. 1(a). Obviously, beam cleaning vanishes whenever the simulation does not include the Kerr effect, i.e., with $n_2 = 0$ [panel (b)]. These numerical simulations are in qualitative agreement with the experimental results of Ref. [11], which were carried out for a slightly different fiber geometry. Figure 3 reveals the evolution with distance of the beam modal composition, corresponding to the case of Fig. 2(a), where $a_{b,k}$ is the amplitude of mode $\psi_{b,k}(x, y)$. Note that the amplitudes $a_{b,k}$ have been numerically calculated via postprocessing at selected coordinates z by projecting the field $E(x, y, z)$ on the eigenmodes $\psi_{b,k}(x, y)$. The eigenmodes $\psi_{b,k}(x, y)$ are the Hermite–Gauss functions, and their definition can be found, for instance, in Refs. [32,33].

Although the signal drops at a rate of 1.9 dB/m , owing to linear losses due to the absence of a pump for inverting the population of the active medium, we still observe that a significant nonlinear power exchange among the modes occurs over the first few meters of propagation. In particular, the blue curve in Fig. 2(a) shows the power carried by the fundamental mode $\psi_{0,0}$, whereas the red and green curves indicate the power carried by modes $\psi_{0,1}$ and $\psi_{1,0}$, respectively: these two modes are poorly excited, because of the symmetry of the input condition. The other modes $\psi_{b,k}$ are plotted in gray (we considered the projections with $b, k \in [0, 9]$).

It is also instructive to calculate the corresponding signal power evolution, as displayed in Fig. 4, where $P_S(z) = \int_S |E(x, y, z)|^2 dS$. It is worth underlining that nonlinear effects occur substantially before the signal is attenuated along its propagation.

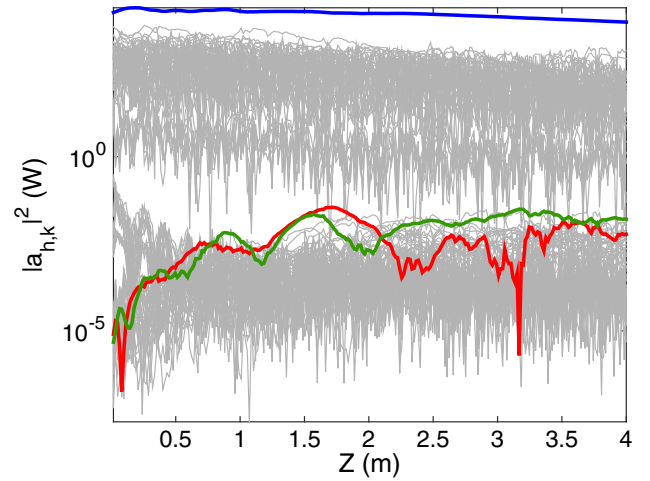


Fig. 3. Beam cleaning in a nonlinear Yb-doped GRIN fiber, in the absence of pump: evolution of the modal power $|a_{b,k}|^2$ ($b, k \in [0, 9]$) in a logarithmic scale for an input signal peak intensity 5 GW/cm^2 (blue line refers to $a_{0,0}$, red to $a_{0,1}$, green to $a_{1,0}$).

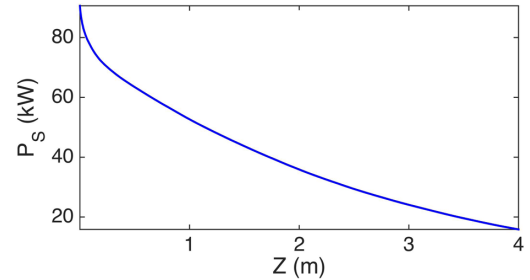


Fig. 4. Signal power along the Yb-doped GRIN fiber in the absence of pump.

4. LINEAR AND NONLINEAR DYNAMICS IN DOPED FIBER WITH FORWARD PUMPING

In this section, we numerically simulate the dynamics of the signal beam amplification when the pump is switched on. The corresponding iso-intensity levels are shown in Fig. 5: as can be seen, for a pump power level of 20 W , beam cleaning is obtained with a signal of 0.5 GW/cm^2 peak intensity only. Note that with such input signal level, it was not possible to obtain beam cleaning in a passive GRIN fiber [see panel (b) of Fig. 1]. To better illustrate this point, Visualization 1 combines a series of simulations when the pump power is varied from 0 to 20 W at constant signal power. We may thus numerically confirm the behavior reported in the experiments of Ref. [11], specifically, a reduction of the input threshold power for beam cleaning in an active fiber, owing to signal amplification, which accompanies nonlinear beam reshaping.

The field gain $g/2$ [as defined in Eq. (4)] experienced by the complex electric field E is neither uniform along the fiber (due to the progressive pump absorption), nor uniform in the transverse domain, owing to the different population inversion across the beam cross section. In particular, gain saturation is most pronounced at the point of minimum waist for the signal beam. The well-known periodic evolution of the beam in a parabolic refractive index profile causes then a periodic fluctuation of the

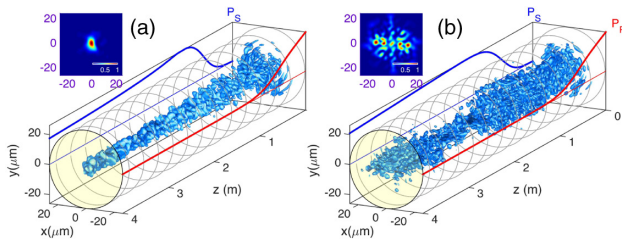


Fig. 5. (a) Beam cleaning in a nonlinear Yb-doped GRIN fiber: forward pump power of 20 W, and input signal peak intensity 0.5 GW/cm^2 ; (b) propagation when turning off the Kerr effect ($n_2 = 0$).

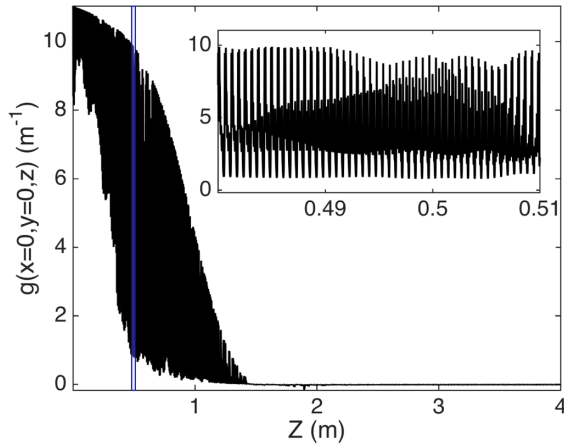


Fig. 6. Signal gain evolution in a nonlinear Yb-doped GRIN fiber: forward pump power of 20 W and input signal peak intensity 0.5 GW/cm^2 . The inset is a zoom of the region highlighted by the blue vertical lines.

signal intensity. In turn, this gives rise to a periodic evolution of the excited ion density $N_2(x, y, z)$ along the coordinate z . To exemplify this effect, in Fig. 6 we show the evolution of the gain along the fiber axis $g(x = 0, y = 0, z)$. The inset is a detail of the evolution over a shorter fiber span, as highlighted by the blue bar. Maximum gain is experienced at the beginning of the propagation, and then gain gradually drops as the pump is absorbed during its propagation. However, the most striking feature of the g evolution is the fast varying oscillation on a submillimetric scale, which is due to the coherent beating of all modes with the self-imaging period of $\Lambda = \pi R / \sqrt{2\Delta}$ (with the present parameters, $\Lambda = 0.6 \text{ mm}$).

A better understanding of the signal dynamics can be gained by observing the evolution of the power carried by the different modes $|a_{h,k}|^2$ (see Fig. 7). Specifically, it is possible to notice that, although all modes are amplified, they clearly have different growth rates. This is surprising, since in the absence of nonlinearity and gain saturation, the uniform doping distribution coupled with the cladding pumping scheme would lead to the same gain per mode. This process culminates in a strong nonlinear reshaping near $z = 1 \text{ m}$.

Along the propagation of the signal beam, amplification increases nonlinear mode mixing and reduces the nonlinear length. As a result, in Fig. 7 we observe a rapid growth of both low- and high-order modes (see for instance the red and green

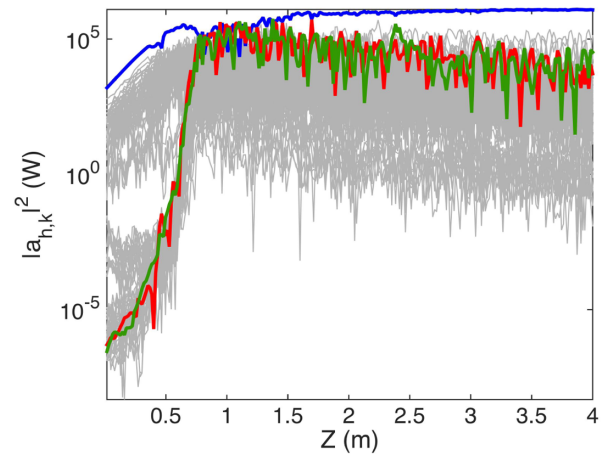


Fig. 7. Beam cleaning in a nonlinear Yb-doped GRIN fiber: mode power evolution on a logarithmic scale. Forward pump of 20 W power, and input signal peak intensity 0.5 GW/cm^2 (the blue line refers to $a_{0,0}$, the red to $a_{0,1}$, and the green to $a_{1,0}$).

curves, referring to modes $a_{0,1}, a_{1,0}$). Note that these very modes are poorly excited in the initial steps of the propagation. In parallel, near $z = 1 \text{ m}$ in Fig. 7, we notice a local decrease of the fundamental mode power (blue curve) before a new amplification stage, which can be ascribed to power flow from high-order modes. Thus, high-order modes can efficiently absorb the gain distributed on the outer edge of the fiber core before transferring it to the fundamental mode by four-wave mixing. For $z > 1 \text{ m}$, the power of the fundamental mode grows larger. Such multistep nonlinear amplification mechanism, involving the amplification of many modes coupled with nonlinear power transfer toward the fundamental mode via the Kerr effect, provides an original light amplification scheme for nonlinear MM fiber amplifiers.

The situation can be possibly clarified by inspecting the evolution of pump and signal powers, as reported in Fig. 8. The strong nonlinear reshaping at $z = 1 \text{ m}$ corresponds to the maximum amplification of the signal, whose peak power reaches above 2.5 MW. Moreover, at that distance, the pump is entirely absorbed, so that over the remaining propagation distance, the signal power is reduced. We can conclude that the Kerr effect may provide an efficient mechanism of nonlinear mode redistribution (especially close to the threshold for beam collapse) and power transfer. We also observed that there is a well-defined optimal amplifier length for obtaining a maximum amplification of the signal.

5. MM ACTIVE TAPERS

An important category of fiber amplifiers is provided by fiber tapers, where both cladding and core radius $R(z)$ vary along the amplifier length. In this section, we support by numerical simulations the results of a series of experiments on nonlinear spectral broadening and beam reshaping in both passive and active MM fiber tapers [34–37]. Here we limit our analysis to the spatial coordinates: in this case, Eq. (3) can be easily extended to tapers, where the radius $R(z)$ varies from a value R_{IN} to a value R_{OUT} . For ease of discussion, we model the evolution of the core radius by means of a linear function

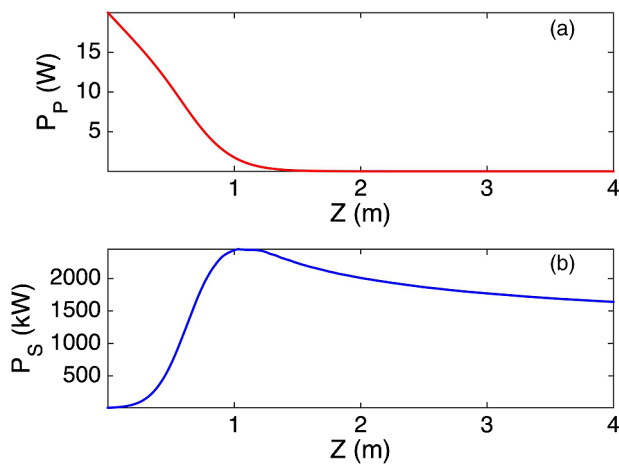


Fig. 8. Powers of (a) pump and (b) signal along the fiber: $\bar{I}_S(0, 0, 0) = 0.5 \text{ GW/cm}^2$ and input pump power $P_P(0) = 20 \text{ W}$.

$R(z) = R_{\text{OUT}} + (z - L)(R_{\text{OUT}} - R_{\text{IN}})/L$, where L is the taper length. In practical implementations of fiber tapers, the variation upon distance of the core radius is not necessarily linear. We refer here to the case $R_{\text{IN}} > R_{\text{OUT}}$, in order to qualitatively reproduce some of the experimental results of Ref. [13]. Note that the decrease of core radius with fiber length progressively increases the strength of the fiber nonlinearity, which leads to an acceleration of nonlinear mixing along the beam propagation [34]. Similar to the previous considered cases, here the pump is combined with the signal in the forward direction. Aiming at a comparative analysis with the previous cases, we considered the same set of parameters' values that we used for uniform or z -invariant fibers. However, in order to match some of the features of the taper of Ref. [13], we have chosen $L = 9 \text{ m}$, $R_{\text{IN}} = 61 \mu\text{m}$, and $R_{\text{OUT}} = 18 \mu\text{m}$. Moreover, in our simulation, the cladding radius linearly varies from $350 \mu\text{m}$ down to $90 \mu\text{m}$. Again, the presence of fiber disorder is introduced by means of local elliptical deformations of the fiber core. Since the core radius changes along the propagation of the signal beam, these deformations are uniformly randomly distributed with a maximal excursion proportional to $R(z)$. In the simulation, the maximal deformation on each axis is $5.8 \times 10^{-3} R(z)$, and with a coarse step of 5 mm .

The numerical simulation presented in Fig. 9 illustrates signal beam propagation along the active taper, in the absence of the Kerr effect (i.e., we set $n_2 = 0$); here the input diode pump power is 20 W , and the signal intensity is 1 GW/cm^2 . As can be seen, the output beam exhibits a speckled intensity pattern. As shown in Fig. 10, the result is qualitatively different when adding the contribution of the Kerr effect. Specifically, the simulation shows that the output signal intensity pattern exhibits a bright spot at its center, surrounded by a weak background. Note that in the considered case, the pump is absorbed over the first meter of fiber, so that for longer distances the signal is experiencing a propagation loss. Nevertheless, Fig. 10 clearly illustrates the gradual transition from a speckled to a cleaned beam when the Kerr effect is switched on.

In fiber amplifiers and lasers, fiber tapers are commonly used by propagating the signal in the opposite direction, namely, with $R_{\text{IN}} < R_{\text{OUT}}$. In fact, if the size of the core increases at the same

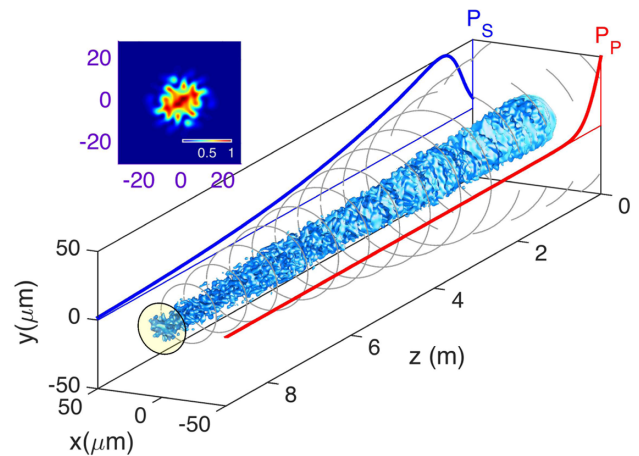


Fig. 9. Iso-intensity surface at half-maximum intensity in a Yb-doped active fiber taper in the absence of Kerr effect ($n_2 = 0$). The blue (red) curve reproduces the evolution of the signal (pump) power. The gray circles represent the local size of the fiber core. The inset shows the output beam intensity pattern.

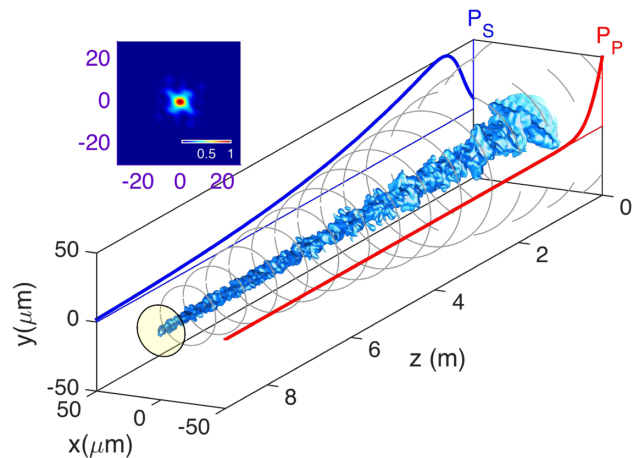


Fig. 10. Same as in Fig. 9, but in the presence of the Kerr effect.

time that the signal is amplified, the nonlinearity increase due to the growing signal power can be compensated by the decrease of the nonlinear coefficient because of the larger effective area of the guided beam. An example of the nonlinear dynamics in this configuration for the MM active taper is illustrated in Fig. 11: here $R_{\text{IN}} = 18 \mu\text{m}$, $R_{\text{OUT}} = 61 \mu\text{m}$, the input beam diameter (FWHMI) is $12.5 \mu\text{m}$, and the input pump power is 20 W . In detail, panel (a) in Fig. 11 illustrates nonlinear propagation in the presence of disorder and the Kerr effect. As can be seen, the signal beam width remains substantially unchanged along the taper, in spite of experiencing a drastic increase of the core diameter. For comparison, panel (b) illustrates propagation in the same taper, but in the absence of the Kerr effect (we set $n_2 = 0$): now, the beam spreads wider along its propagation. Although the present simulations refer to a forward pumping situation, these numerical results substantially agree with the experimental observations of spatial BSC in active tapers with decelerating nonlinearity, as reported in Ref. [14], and obtained with a backward pump.

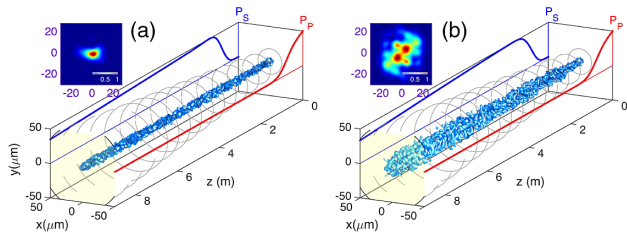


Fig. 11. Numerical simulation of nonlinear beam propagation in a Yb-doped fiber taper with $R_{IN} = 18.5 \mu\text{m}$ and $R_{OUT} = 61 \mu\text{m}$ (the signal propagation direction is inverted with respect to Figs. 9 and 10). (a) In the presence of the Kerr effect; (b) in the absence of the Kerr effect ($n_2 = 0$).

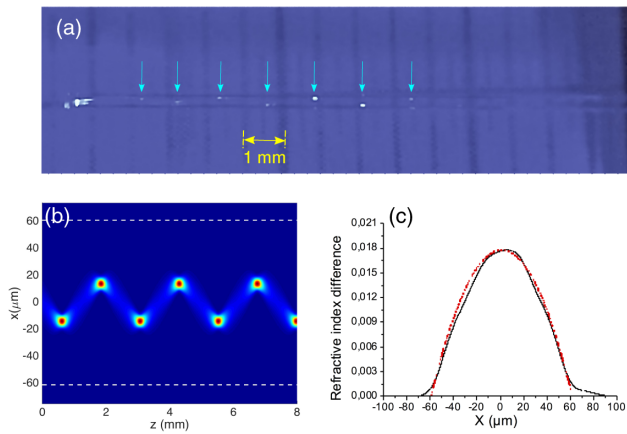


Fig. 12. (a) Photoluminescence measured by using a pulsed laser at 1030 nm for a short taper segment with a fiber radius $R = 61 \mu\text{m}$; (b) numerically calculated intensity evolution in a uniform fiber with core radius $R = 61 \mu\text{m}$; (c) measured local refractive index profile.

Since core and cladding radii vary slowly along the taper, a significant change of their values can only be obtained after a distance that is orders of magnitude greater than the typical value of the self-imaging period (which ranges from a few millimeters to a few hundred micrometers). For this reason, the self-imaging effect can also be observed in short segments of the taper in Fig. 10. Since the period Λ is proportional to the core radius R [31], self-imaging accelerates (i.e., Λ decreases) when going from the large core input facet ($\Lambda \sim 1.3 \text{ mm}$) to the small core one ($\Lambda \sim 0.4 \text{ mm}$).

As an example, we may consider the Yb-doped fiber that was used in Ref. [13]. Panel (a) of Fig. 12 shows the experimental photoluminescence that is observed at points where the maxima of intensity are reached: here the spacing between two consecutive points is 1.2 mm. These results are obtained by using an experimental setup that is similar to that described in Refs. [35–38]. Panel (b) shows the calculated intensity evolution along a uniform fiber segment, i.e., with constant radius $R = 61 \mu\text{m}$ and a parabolic refractive index profile corresponding to the experimental profile in panel (c). In such a case, the input Gaussian beam is injected off-axis, and the corresponding intensity distribution exhibits a zigzag trajectory with a period of 2Λ . As a matter of fact, Λ is the self-imaging period for an on-axis symmetric input field only, similar to what is observed in other MM waveguides [39,40]. Note that these zigzag trajectories in

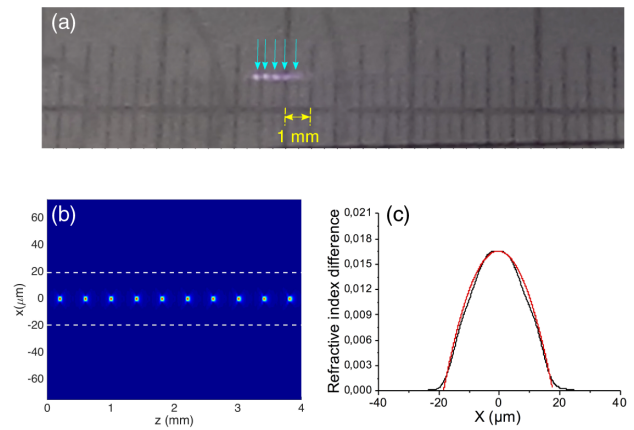


Fig. 13. (a) Photoluminescence measured by using a pulsed laser at 1030 nm for a short taper segment with a fiber radius $R = 19.5 \mu\text{m}$; (b) numerically calculated intensity evolution in a uniform fiber having core radius $R = 19.5 \mu\text{m}$; (c) measured local refractive index profile.

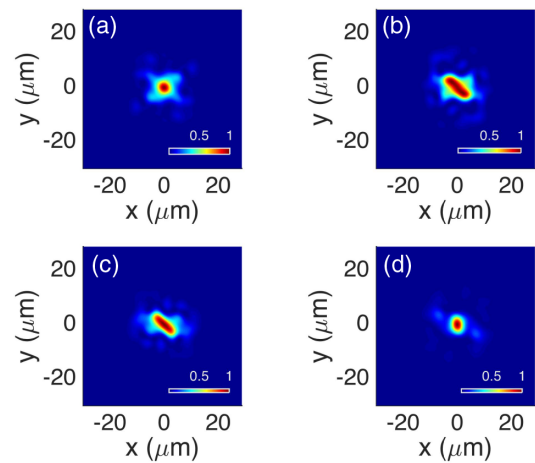


Fig. 14. Beam shapes at the output of the fiber taper with different strengths of refractive index perturbation δn , caused by the population inversion of Yb ions. (a) $\delta n = 1 \times 10^{-6} N_2/N_T$; (b) $\delta n = 4 \times 10^{-6} N_2/N_T$; (c) $\delta n = 6 \times 10^{-6} N_2/N_T$; (d) $\delta n = 9 \times 10^{-6} N_2/N_T$. The remaining parameters are those of Fig. 10.

nonlinear GRIN fibers have been studied, with a variational method, in Ref. [41]. With $R = 61 \mu\text{m}$, $\Delta n = 0.018$ and assuming, for instance, $n_{Cl} = 1.457$, the calculated self-imaging period is $\Lambda = 1.2 \text{ mm}$: this value is close to the experimental result in Fig. 12(a), and agrees well with the numerical result in Fig. 12(b).

The signal beam intensity maxima are more closely packed when observing the taper near its small input facet, as illustrated in Fig. 13: here panel (a) shows the light scattered by photoluminescence. As can be seen, the spacing between two consecutive bright spots reduces to 0.36 mm, owing to the reduced diameter, whereas panel (b) illustrates the numerical propagation result, again assuming a segment of constant diameter for a few millimeters of propagation, and panel (c) shows the corresponding measured local refractive index profile. With $R = 19.5 \mu\text{m}$, $\Delta n = 0.017$, and $n_{Cl} = 1.457$, the expected self-imaging period is $\Lambda = 0.4 \text{ mm}$. These experimental results agree well with the numerical ones, and with the self-imaging

theory, thus extending the analysis presented in Refs. [35–37] from standard 50/125 GRIN MM fibers to the case of Yb-doped MM tapers.

At this point, we may briefly address the relevant problem of the local refractive index perturbations that are induced by the population inversion in the active fiber medium. Figure 14 analyzes the additional impact of the refractive index perturbation δn , which is caused by the population inversion of Yb ions, as described by Eq. (5). Here we show the output beam profiles for realistic values of δn . The simulations have been carried out with the same parameters as in Fig. 10. To simplify our analysis, δn is assumed to be proportional to the ratio N_2/N_T , with a proportionality factor ranging from 1×10^{-6} [panel (a)] up to 9×10^{-6} [panel (d)]. The conclusion of this analysis is that, although population inversion can induce a refractive index perturbation, its impact is not sufficient to reduce the effectiveness of spatial beam cleaning, at least within the considered range of parameters.

6. CONCLUSION

In this work, we carried out a series of numerical simulations in order to study the onset of nonlinear beam reshaping and cleaning in MM GRIN fiber amplifiers. At variance with single-mode fibers, GRIN fibers lead to a periodic evolution of the signal intensity, which, in turn, periodically modulates the population inversion. The beam-cleaning effects observed in our numerical simulations agree well with experimentally reported spatial BSC in Refs. [11–14] and add a new building block to the study of this interesting nonlinear phenomenon. In this work, as well as in the reported experiments, we have shown how BSC can be observed even in dissipative fiber systems, where the signal power evolves (under the effect of either linear absorption or amplification), namely, in the absence of conservation of the signal power. Peculiar properties of the associated nonlinear beam evolution have been pointed out, specifically in connection with the contribution of the active medium, and its nonuniform transverse population distribution, whose detailed analysis deserves further studies.

Funding. ArianeGroup (CILAS X-LAS); H2020 European Research Council (740355); Narodowa Agencja Wymiany Akademickiej (BPN/BFR/2021/1/00013); Campus France (48161TH).

Acknowledgment. We acknowledge useful discussions and suggestions by Dr. Alain Barthélemy.

Disclosures. The authors declare no conflicts of interest.

Data availability. Data underlying the results presented in this paper are not publicly available at this time but may be obtained from the authors upon reasonable request.

REFERENCES

1. A. E. Siegman, "Gain-guided, index-antiguidded fiber lasers," *J. Opt. Soc. Am. B* **24**, 1677–1682 (2007).
2. G. P. Agrawal, "Optical pulse propagation in doped fiber amplifiers," *Phys. Rev. A* **44**, 7493–7501 (1991).
3. R. Lindberg, P. Zeil, M. Malmström, F. Laurell, and V. Pasiskevicius, "Accurate modeling of high-repetition rate ultrashort pulse amplification in optical fibers," *Sci. Rep.* **6**, 34742 (2016).
4. K. R. Hansen, T. T. Alkeskjold, J. Broeng, and J. Lægsgaard, "Thermo-optical effects in high-power ytterbium-doped fiber amplifiers," *Opt. Express* **19**, 23965–23980 (2011).
5. J. Lægsgaard, F. Poli, A. Cucinotta, and S. Selleri, "Static and dynamic mode instabilities in dual-core fiber amplifiers," *J. Opt. Soc. Am. B* **36**, 757–767 (2019).
6. C. Stihler, C. Jauregui, A. Tünnermann, and J. Limpert, "Modal energy transfer by thermally induced refractive index gratings in Yb-doped fibers," *Light Sci. Appl.* **7**, 59 (2018).
7. C. Jauregui, T. Eidam, J. Limpert, and A. Tünnermann, "Impact of modal interference on the beam quality of high-power fiber amplifiers," *Opt. Express* **19**, 3258–3271 (2011).
8. R. Florentin, V. Kermene, A. Desfarges-Berthelemot, and A. Barthélemy, "Shaping of amplified beam from a highly multimode Yb-doped fiber using transmission matrix," *Opt. Express* **27**, 32638–32648 (2019).
9. R. Florentin, V. Kermene, J. Benoist, A. Desfarges-Berthelemot, D. Pagnoux, A. Barthélemy, and J.-P. Huignard, "Shaping the light amplified in a multimode fiber," *Light Sci. Appl.* **6**, e16208 (2017).
10. K. Krupa, A. Tonello, B. M. Shalaby, M. Fabert, A. Barthélemy, G. Millot, S. Wabnitz, and V. Couderc, "Spatial beam self-cleaning in multimode fibres," *Nat. Photonics* **11**, 237–241 (2017).
11. R. Guenard, K. Krupa, R. Dupiol, M. Fabert, A. Bendahmane, V. Kermene, A. Desfarges-Berthelemot, J. L. Auguste, A. Tonello, A. Barthélemy, G. Millot, S. Wabnitz, and V. Couderc, "Kerr self-cleaning of pulsed beam in an ytterbium doped multimode fiber," *Opt. Express* **25**, 4783–4792 (2017).
12. R. Guenard, K. Krupa, R. Dupiol, M. Fabert, A. Bendahmane, V. Kermene, A. Desfarges-Berthelemot, J. L. Auguste, A. Tonello, A. Barthélemy, G. Millot, S. Wabnitz, and V. Couderc, "Nonlinear beam self-cleaning in a coupled cavity composite laser based on multimode fiber," *Opt. Express* **25**, 22219–22227 (2017).
13. A. Niang, T. Mansuryan, K. Krupa, A. Tonello, M. Fabert, P. Leproux, D. Modotto, O. N. Egorova, A. E. Levchenko, D. S. Lipatov, S. L. Semjonov, G. Millot, V. Couderc, and S. Wabnitz, "Spatial beam self-cleaning and supercontinuum generation with Yb-doped multimode graded-index fiber taper based on accelerating self-imaging and dissipative landscape," *Opt. Express* **27**, 24018–24028 (2019).
14. A. Niang, D. Modotto, A. Tonello, F. Mangini, U. Minoni, M. Zitelli, M. Fabert, M. A. Jima, O. N. Egorova, A. E. Levchenko, S. L. Semjonov, D. S. Lipatov, S. Babin, V. Couderc, and S. Wabnitz, "Spatial beam self-cleaning in tapered Yb-doped grn multimode fiber with decelerating nonlinearity," *IEEE Photon. J.* **12**, 6500308 (2020).
15. A. Fusaro, J. Garnier, K. Krupa, G. Millot, and A. Picozzi, "Dramatic acceleration of wave condensation mediated by disorder in multimode fibers," *Phys. Rev. Lett.* **122**, 123902 (2019).
16. J. Garnier, A. Fusaro, K. Baudin, C. Michel, K. Krupa, G. Millot, and A. Picozzi, "Wave condensation with weak disorder versus beam self-cleaning in multimode fibers," *Phys. Rev. A* **100**, 053835 (2019).
17. F. O. Wu, A. U. Hassan, and D. N. Christodoulides, "Thermodynamic theory of highly multimoded nonlinear optical systems," *Nat. Photonics* **13**, 776–782 (2019).
18. E. V. Podivilov, D. S. Kharenko, V. A. Gonta, K. Krupa, O. S. Sidelnikov, S. Turitsyn, M. P. Fedoruk, S. A. Babin, and S. Wabnitz, "Hydrodynamic 2D turbulence and spatial beam condensation in multimode optical fibers," *Phys. Rev. Lett.* **122**, 103902 (2019).
19. K. Baudin, A. Fusaro, K. Krupa, J. Garnier, S. Rica, G. Millot, and A. Picozzi, "Classical Rayleigh-Jeans condensation of light waves: observation and thermodynamic characterization," *Phys. Rev. Lett.* **125**, 244101 (2020).
20. H. Pourbeyram, P. Sidorenko, F. O. Wu, N. Bender, L. Wright, D. N. Christodoulides, and F. Wise, "Direct observations of thermalization to a Rayleigh-Jeans distribution in multimode optical fibres," *Nat. Phys.* **18**, 685–690 (2022).
21. F. Mangini, M. Gervaziev, M. Ferraro, D. S. Kharenko, M. Zitelli, Y. Sun, V. Couderc, E. V. Podivilov, S. A. Babin, and S. Wabnitz, "Statistical mechanics of beam self-cleaning in GRIN multimode optical fibers," *Opt. Express* **30**, 10850–10865 (2022).
22. L. G. Wright, D. N. Christodoulides, and F. W. Wise, "Spatiotemporal mode-locking in multimode fiber lasers," *Science* **358**, 94–97 (2017).

23. U. Tegin, B. Rahmani, E. Kakkava, D. Psaltis, and C. Moser, "Single-mode output by controlling the spatiotemporal nonlinearities in mode-locked femtosecond multimode fiber lasers," *Adv. Photon.* **2**, 056005 (2020).
24. U. Teğın, E. Kakkava, B. Rahmani, D. Psaltis, and C. Moser, "Spatiotemporal self-similar fiber laser," *Optica* **6**, 1412–1415 (2019).
25. K. Krupa, G. G. Castañeda, A. Tonello, A. Niang, D. S. Kharenko, M. Fabert, V. Couderc, G. Millot, U. Minoni, D. Modotto, and S. Wabnitz, "Nonlinear polarization dynamics of Kerr beam self-cleaning in a graded-index multimode optical fiber," *Opt. Lett.* **44**, 171–174 (2019).
26. A. A. Runge, C. Aguergaray, R. Provo, M. Erkintalo, and N. G. Broderick, "All-normal dispersion fiber lasers mode-locked with a nonlinear amplifying loop mirror," *Opt. Fiber Technol.* **20**, 657–665 (2014).
27. A. A. Fotiadi, O. L. Antipov, and P. Mégret, "Resonantly induced refractive index changes in yb-doped fibers: the origin, properties and application for all-fiber coherent beam combining," in *Frontiers in Guided Wave Optics and Optoelectronics* (2010), pp. 209–234.
28. H. M. Pask, R. J. Carman, D. C. Hanna, A. C. Tropper, C. J. Mackechnie, P. R. Barber, and J. M. Dawes, "Ytterbium-doped silica fiber lasers: versatile sources for the 1–1.2 μm region," *IEEE J. Sel. Top. Quantum Electron.* **1**, 2–13 (1995).
29. R. Paschotta, J. Nilsson, A. C. Tropper, and D. C. Hanna, "Ytterbium-doped fiber amplifiers," *IEEE J. Quantum Electron.* **33**, 1049–1056 (1997).
30. S. Longhi, "Modulational instability and space-time dynamics in nonlinear parabolic-index optical fibers," *Opt. Lett.* **28**, 2363–2365 (2003).
31. G. P. Agrawal, "[Invite paper]: Self-imaging in multimode graded-index fibers and its impact on the nonlinear phenomena," *Opt. Fiber Technol.* **50**, 309–316 (2019).
32. A. Ghatak and K. Thyagarajan, "Propagation characteristics of graded index fibers," in *Introduction to Fiber Optics* (Cambridge University, 1998), Chap. 9.
33. M. B. Shemirani, W. Mao, R. A. Panicker, and J. M. Kahn, "Principal modes in graded-index multimode fiber in presence of spatial- and polarization-mode coupling," *J. Lightwave Technol.* **27**, 1248–1261 (2009).
34. M. A. Eftekhar, Z. Sanjabi-Eznaveh, H. E. Lopez-Aviles, S. Benis, J. E. Antonio-Lopez, M. Kolesik, F. Wise, R. Amezcua-Correa, and D. N. Christodoulides, "Accelerated nonlinear interactions in graded-index multimode fibers," *Nat. Commun.* **10**, 1638 (2019).
35. K. Krupa, A. Tonello, A. Barthélémy, T. Mansuryan, V. Couderc, G. Millot, P. Grelu, D. Modotto, S. A. Babin, and S. Wabnitz, "Multimode nonlinear fiber optics, a spatiotemporal avenue," *APL Photon.* **4**, 110901 (2019).
36. T. Hansson, A. Tonello, T. Mansuryan, F. Mangini, M. Zitelli, M. Ferraro, A. Niang, R. Crescenzi, S. Wabnitz, and V. Couderc, "Nonlinear beam self-imaging and self-focusing dynamics in a grin multimode optical fiber: theory and experiments," *Opt. Express* **28**, 24005–24021 (2020).
37. F. Mangini, M. Ferraro, M. Zitelli, A. Niang, A. Tonello, V. Couderc, and S. Wabnitz, "Multiphoton-absorption-excited up-conversion luminescence in optical fibers," *Phys. Rev. Appl.* **14**, 054063 (2020).
38. M. Ferraro, F. Mangini, Y. Sun, M. Zitelli, A. Niang, M. C. Crocco, V. Formoso, R. G. Agostino, R. Barberi, A. D. Luca, A. Tonello, V. Couderc, S. A. Babin, and S. Wabnitz, "Multiphoton ionization of standard optical fibers," *Photon. Res.* **10**, 1394–1400 (2022).
39. M. Bachmann, P. A. Besse, and H. Melchior, "General self-imaging properties in $n \times n$ multimode interference couplers including phase relations," *Appl. Opt.* **33**, 3905–3911 (1994).
40. M. Bachmann, P. A. Besse, and H. Melchior, "Overlapping-image multimode interference couplers with a reduced number of self-images for uniform and nonuniform power splitting," *Appl. Opt.* **34**, 6898–6910 (1995).
41. C.-H. Chien, S.-S. Yu, Y. Lai, and J. Wang, "Off-axial pulse propagation in graded-index materials with Kerr nonlinearity—a variational approach," *Opt. Commun.* **128**, 145–157 (1996).